

Influence of substrate effect on near-field radiative modulator based on biaxial hyperbolic materials

Ruiyi Liu(刘睿一), Haotuo Liu(刘皓佗), Yang Hu(胡杨), Zheng Cui(崔峥), and Xiaohu Wu(吴小虎)

Citation: Chin. Phys. B, 2024, 33 (**4**): 044403. DOI: 10.1088/1674-1056/ad2a6c
Journal homepage: http://cpb.iphy.ac.cn; http://iopscience.iop.org/cpb

What follows is a list of articles you may be interested in

Preparation and cooling performance analysis of double-layer radiative cooling hybrid coatings with $TiO_2/SiO_2/Si_3N_4$ micron particles

Yang-Chun Zhao(赵洋春) and Yong-Min Zhou(周勇敏)
Chin. Phys. B, 2023, 32 (**11**): 114401. DOI: 10.1088/1674-1056/acdac0

Tuning infrared absorption in hyperbolic polaritons coated silk fibril composite

Lihong Shi(史丽弘) and Jiebin Peng(彭洁彬)
Chin. Phys. B, 2022, 31 (**11**): 114401. DOI: 10.1088/1674-1056/ac8cdc

Calculation of radiative heat flux on irregular boundaries in participating media

Yu-Jia Sun(孙玉佳) and Shu Zheng(郑树)
Chin. Phys. B, 2020, 29 (**12**): 124401. DOI: 10.1088/1674-1056/abb22a

Infrared cooling properties of cordierite

Si-Heng Chen(陈思衡), Xiao-Xiong Wang(王晓雄), Guang-Di Nie(乜广弟), Qi Liu(刘奇), Jin-Xia Sui(隋金霞), Chao Song(宋超), Jian-Wei Zhu(朱建伟), Jie Fu(付洁), Jun-Cheng Zhang(张君诚), Xu Yan(闫旭), Yun-Ze Long(龙云泽)
Chin. Phys. B, 2019, 28 (**6**): 064401. DOI: 10.1088/1674-1056/28/6/064401

Contribution of terahertz waves to near-field radiative heat transfer between graphene-based hyperbolic metamaterials

Qi-Mei Zhao(赵启梅), Tong-Biao Wang(王同标), De-Jian Zhang(张德建), Wen-Xing Liu(刘文兴), Tian-Bao Yu(于天宝), Qing-Hua Liao(廖清华), Nian-Hua Liu(刘念华)
Chin. Phys. B, 2018, 27 (**9**): 094401. DOI: 10.1088/1674-1056/27/9/094401

SPECIAL TOPIC — Heat conduction and its related interdisciplinary areas

Influence of substrate effect on near-field radiative modulator based on biaxial hyperbolic materials

Ruiyi Liu(刘睿一)[1], Haotuo Liu(刘皓佗)[2], Yang Hu(胡杨)[3], Zheng Cui(崔峥)[2,†], and Xiaohu Wu(吴小虎)[2,‡]

[1] *Institute of Advanced Technology, Shandong University, Jinan* 250061, *China*
[2] *Shandong Institute of Advanced Technology, Jinan* 250100, *China*
[3] *School of Power and Energy, Northwestern Polytechnical University, Xi'an* 710072, *China*

(Received 21 November 2023; revised manuscript received 29 January 2024; accepted manuscript online 19 February 2024)

Relative rotation between the emitter and receiver could effectively modulate the near-field radiative heat transfer (NFRHT) in anisotropic media. Due to the strong in-plane anisotropy, natural hyperbolic materials can be used to construct near-field radiative modulators with excellent modulation effects. However, in practical applications, natural hyperbolic materials need to be deposited on the substrate, and the influence of substrate on modulation effect has not been studied yet. In this work, we investigate the influence of substrate effect on near-field radiative modulator based on α-MoO_3. The results show that compared to the situation without a substrate, the presence of both lossless and lossy substrate will reduce the modulation contrast (MC) for different film thicknesses. When the real or imaginary component of the substrate permittivity increases, the mismatch of hyperbolic phonon polaritons (HPPs) weakens, resulting in a reduction in MC. By reducing the real and imaginary components of substrate permittivity, the MC can be significantly improved, reaching 4.64 for $\varepsilon_s = 3$ at $t = 10$ nm. This work indicates that choosing a substrate with a smaller permittivity helps to achieve a better modulation effect, and provides guidance for the application of natural hyperbolic materials in the near-field radiative modulator.

Keywords: near-field radiative modulator, substrate effect, hyperbolic material, modulation contrast

PACS: 44.40.+a, 78.20.–e, 71.36.+c, 78.20.Bh **DOI:** 10.1088/1674-1056/ad2a6c

1. Introduction

At the nanoscale, the coupling of evanescent modes introduces new pathways for heat transfer.[1,2] Photon tunneling through evanescent modes significantly enhances the near-field radiative heat transfer (NFRHT), enabling it to far exceed the blackbody limit.[3–29] The advancement of NFRHT has garnered considerable attention because of its potential in applications like thermophotovoltaics,[30–36] thermal rectification,[37–39] solid-state cooling,[40–42] and so on.

Recently, near-field radiative modulator has become a focus of attention due to its role in thermal information processing and thermal management. Various methods for modulating the NFRHT have been proposed, including the use of phase-change materials,[43] magnetic-optical materials,[44] and bias voltage tuning.[45] In 2011, Biehs *et al.*[46] proposed applying relative rotation between the receiver and emitter to modulate the NFRHT, which has sparked many studies on near-field radiative modulators utilizing planar anisotropic media.[47–54] Natural hyperbolic materials are characterized by their principal permittivity components, which have opposite signs,[55,56] so the excited hyperbolic phonon polaritons (HPPs) exhibit in-plane anisotropy characteristics and can be used for rotational modulation of the NFRHT. Liu *et al.* proposed using rotated hBN films to modulate the NFRHT, due to the mismatching HPPs induced by rotation, the modulation contrast (MC) could be more than 5.[52] Wu *et al.* explored a near-field radiative modulator utilizing hBN and α-MoO_3, achieving a maximum MC of 12.45.[53] Li *et al.* investigated the NFRHT between rotated α-MoO_3 films, achieving a heat flux 36 times greater than the blackbody limit and an MC of up to 6.33.[54] In these studies, the natural hyperbolic material thin films are assumed to be suspended. However, in practical application, natural hyperbolic materials need to be deposited on the substrate.[8,57–59] Considering the application condition of thermal modulators, it is necessary to clarify the influence of substrate on modulation effect, which has not been studied yet.

As a biaxial hyperbolic material and displaying pronounced in-plane anisotropy, α-MoO_3 shows great potential in modulating the NFRHT. Here, we investigate the NFRHT between α-MoO_3 films backed by both lossless and lossy substrates, and discuss the influence of variations in the real and imaginary components of substrate permittivity on the MC. By calculating the spectral heat flux (SHF), we analyze the reasons for the differences in NFRHT before and after rotation. Additionally, we plot the reflection coefficient and energy transmission coefficient (ETC) to reveal the underlying physical mechanisms. This study provides guidelines for the selection of substrate and practical application of natural hy-

†Corresponding author. E-mail: zhengc@sdu.edu.cn
‡Corresponding author. E-mail: xiaohu.wu@iat.cn

© 2024 Chinese Physical Society and IOP Publishing Ltd

perbolic materials in near-field radiative modulators.

2. Model and methods

Figure 1 illustrates the model structure, it consists of two α-MoO_3 films, each backed by a bulk substrate, and there is a vacuum gap between them with a distance of $d = 100$ nm. The receiver rotates at an angle γ relative to the emitter. We consider the case of NFRHT following three crystal orientations of α-MoO_3, respectively. Here, the temperatures are $T_1 = 330$ K for the emitter and $T_2 = 300$ K for the receiver. The thickness of the α-MoO_3 film is t, and the substrate permittivity is ε_s.

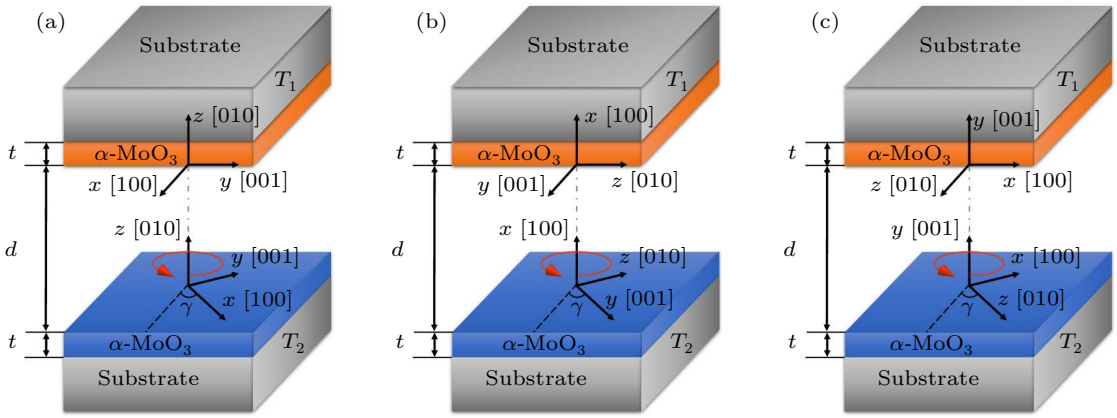


Fig. 1. Schematic diagrams of the near-field radiative modulator. The NFRHT follows (a) [010], (b) [100], and (c) [001] crystal orientations of α-MoO_3.

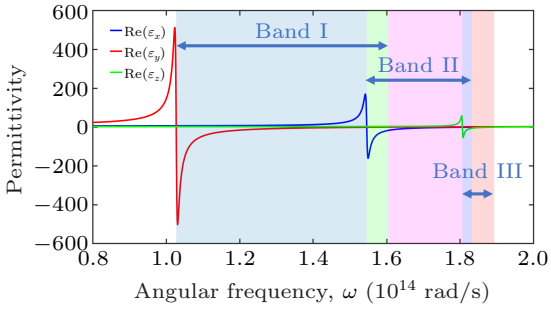


Fig. 2. The real components of relative permittivity of α-MoO_3. The three reststrahlen bands are indicated by distinct shaded areas.

The expression for the relative permittivity of α-MoO_3 is[56]

$$\varepsilon_m(\omega) = \varepsilon_{\infty,m}\left(1 + \frac{\omega_{\mathrm{LO},m}^2 - \omega_{\mathrm{TO},m}^2}{\omega_{\mathrm{TO},m}^2 - \omega^2 - \mathrm{j}\omega\Gamma_m}\right), \tag{1}$$

where ω is the angular frequency. The three directions of parameters are $m = x$, y, and z, the specific parameters are $\omega_{\mathrm{LO},x} = 1.8322 \times 10^{14}$ rad/s, $\omega_{\mathrm{LO},y} = 1.6041 \times 10^{14}$ rad/s, $\omega_{\mathrm{LO},z} = 1.8925 \times 10^{14}$ rad/s, $\omega_{\mathrm{TO},x} = 1.5457 \times 10^{14}$ rad/s, $\omega_{\mathrm{TO},y} = 1.0273 \times 10^{14}$ rad/s, $\omega_{\mathrm{TO},z} = 1.8058 \times 10^{14}$ rad/s, $\varepsilon_{\infty,x} = 4$, $\varepsilon_{\infty,y} = 5.2$, $\varepsilon_{\infty,z} = 2.4$, $\Gamma_x = 7.5398 \times 10^{11}$ s^{-1}, $\Gamma_y = 7.5398 \times 10^{11}$ s^{-1} and $\Gamma_z = 3.7699 \times 10^{11}$ s^{-1}.[56] Figure 2 plots the real components of relative permittivity of α-MoO_3, which show negative values in three reststrahlen bands indicated by distinct shaded regions.

In the situation of optical axis tilted by an angle of γ, the permittivity changes to[55]

$$\begin{pmatrix} \cos\gamma & -\sin\gamma & 0 \\ \sin\gamma & \cos\gamma & 0 \\ 0 & 0 & 1 \end{pmatrix} \varepsilon \begin{pmatrix} \cos\gamma & \sin\gamma & 0 \\ -\sin\gamma & \cos\gamma & 0 \\ 0 & 0 & 1 \end{pmatrix}. \tag{2}$$

The calculation of NFRHT between high-temperature medium 1 and low-temperature medium 2 can be determined by[60]

$$Q = \frac{1}{8\pi^3}\int_0^\infty [\Theta(\omega, T_1) - \Theta(\omega, T_2)]\,\mathrm{d}\omega \times \int_0^{2\pi}\int_0^\infty \xi(\omega, \beta, \phi)\,\beta\,\mathrm{d}\beta\,\mathrm{d}\phi, \tag{3}$$

where $\Theta(\omega, T) = \hbar\omega/\left(\mathrm{e}^{\hbar\omega/k_\mathrm{B}T} - 1\right)$ is the average energy of a Planck oscillator, $\xi(\omega, \beta, \phi)$ is the ETC, and it is expressed as[60]

$$\xi(\omega, \beta, \varphi) = \begin{cases} \mathrm{Tr}\left[(\boldsymbol{I} - \boldsymbol{R}_2^*\boldsymbol{R}_2 - \boldsymbol{T}_2^*\boldsymbol{T}_2)\,\boldsymbol{D}\,(\boldsymbol{I} - \boldsymbol{R}_1^*\boldsymbol{R}_1 - \boldsymbol{T}_1^*\boldsymbol{T}_1)\,\boldsymbol{D}^*\right], & \beta < k_0, \\ \mathrm{Tr}\left[(\boldsymbol{R}_2^* - \boldsymbol{R}_2)\,\boldsymbol{D}\,(\boldsymbol{R}_1 - \boldsymbol{R}_1^*)\,\boldsymbol{D}^*\right]\mathrm{e}^{-2|k_z|d}, & \beta > k_0, \end{cases} \tag{4}$$

where k_0 is the vacuum wavevector. $\boldsymbol{I}$ is a 2×2 unit matrix and $\boldsymbol{D} = \left(\boldsymbol{I} - \boldsymbol{R}_1\boldsymbol{R}_2\,\mathrm{e}^{-2\mathrm{j}k_z d}\right)^{-1}$. $\boldsymbol{R}$ and $\boldsymbol{T}$ are characterized as follows:[55]

$$\boldsymbol{R}_{1,2} = \begin{bmatrix} r_{\mathrm{ss}}^{(1,2)} & r_{\mathrm{sp}}^{(1,2)} \\ r_{\mathrm{ps}}^{(1,2)} & r_{\mathrm{pp}}^{(1,2)} \end{bmatrix}, \quad \boldsymbol{T}_{1,2} = \begin{bmatrix} t_{\mathrm{ss}}^{(1,2)} & t_{\mathrm{sp}}^{(1,2)} \\ t_{\mathrm{ps}}^{(1,2)} & t_{\mathrm{pp}}^{(1,2)} \end{bmatrix}, \tag{5}$$

where r and t are reflection and transmission coefficients from vacuum to medium 1 or 2, the first and second letters of the subscript in each coefficient represent the polarization states of the incident and reflected waves, the detailed parameters are available in Ref. [55].

3. Results and discussion

3.1. Substrate effect of lossless substrate

Firstly, we consider the impact of the lossless substrate on the MC, as depicted in Fig. 3. Figure 3(a) illustrates the variation of MC with thickness when NFRHT follows [010] crystal orientation of α-MoO_3. It can be observed that the MC, defined as $Q(0^\circ)/Q(90^\circ)$, attains its peak value of 6.35 at $t = 10$ nm when $\varepsilon_s = 1$ (i.e., without substrate). After reaching its maximum value, the MC decreases with increasing film thickness when $t > 10$ nm. As for lossless substrate ($\varepsilon_s = 3$, 5, and 10), the MC obviously decreases relative to that of $\varepsilon_s = 1$, and the MC continues to decrease with the increase of ε_s. There is a maximum value of the MC (4.64) at $t = 10$ nm when $\varepsilon_s = 3$, then the MC decreases with film thickness. For the case of $\varepsilon_s = 5$ and 10, the MC monotonically increases with film thickness. The MCs vary with film thickness at small thicknesses, and tend to remain stable as the film thickness approaches 100 nm. This phenomenon is attributed to the evanescent mode which dominates the NFRHT, has a penetration depth of approximately d (100 nm in this case).[61–63] As the film thickness approaches or exceeds the penetration depth, the film can absorb most radiative energy. Consequently, the NFRHT becomes less sensitive to further variation in film thickness, leading to a stabilization of the MC.

As shown in Fig. 3(b), when NFRHT follows [100] crystal orientation of α-MoO_3, the variation trend of MC with different ε_s is similar to that of the [010] case, only the amplitude of variation is greater. However, in Fig. 3(c), when NFRHT follows [001] crystal orientation of α-MoO_3, the variation of MC exhibits an opposite trend. When $\varepsilon_s = 1$, the MC reaches its minimum value at $t = 10$ nm, then increases with film thickness and stabilizes when t approaches the penetration depth of approximately d (100 nm in this case). Besides, the MC with lossless substrate monotonically increases with film thickness, and the difference between the MCs with different lossless substrates is not significant. Detailed analyses of the variation of MC with film thickness for different heat transfer directions are presented in the supplementary material. It can be seen that regardless of the orientation of NFRHT, the presence of lossless substrate will reduce the MC compared to the case without substrate, and the reduction in MC becomes more pronounced as ε_s increases. In other words, the smaller the ε_s, the larger the MC can be obtained. In the following discussion, we will use the example of NFRHT following [010] crystal orientation of α-MoO_3, to analyze the reasons for the impact of lossless substrate on MC.

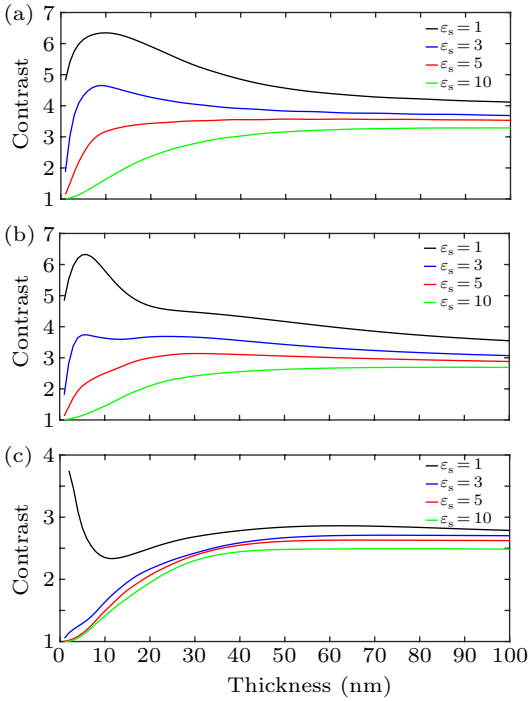


Fig. 3. Variation in modulation contrast with α-MoO_3 film thickness when NFRHT follows (a) [010], (b) [100], and (c) [001] crystal orientations. The substrate permittivities are $\varepsilon_s = 1$, 3, 5, and 10.

To explain the differences in the MCs with different ε_s, we discuss the variation in heat flux with rotation angle γ, as depicted in Fig. 4. The thickness of α-MoO_3 films is set to $t = 10$ nm, for the difference between the MCs with different ε_s is significant at this thickness. As the rotation angle increases, there is a rapid decrease in total heat flux at small rotation angles, followed by a slower decline as the rotation angle continues to grow. When $\gamma = 90^\circ$, the heat flux for different substrate permittivities decreases to around 1 kW/m^2, with little difference. When $\gamma = 0^\circ$, the heat flux for $\varepsilon_s = 1$ is obviously larger than other cases, reaching 7.17 kW/m^2, resulting in a higher MC. As ε_s increases, the heat flux at $\gamma = 0^\circ$ gradually decreases, thus the MC decreases. It is noteworthy that when $\varepsilon_s = 10$, the heat flux is relatively high at large rotation angles, and even exceeds that for $\varepsilon_s = 1$ at $\gamma = 90^\circ$, resulting in a small difference between the heat fluxes at $\gamma = 0^\circ$ and $\gamma = 90^\circ$. Therefore, the MC for $\varepsilon_s = 10$ is very small.

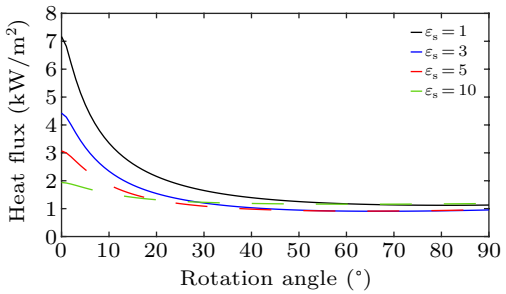


Fig. 4. Variation in heat flux with rotation angle. The substrate permittivities are $\varepsilon_s = 1$, 3, 5, and 10. $t = 10$ nm.

Furthermore, in Fig. 5 we analyze the SHF at $\gamma = 0°$ and $\gamma = 90°$ for different ε_s, to investigate the reasons for the differences in total heat flux before and after rotation. For the case of $\varepsilon_s = 1$, there is a huge difference between the SHFs at $\gamma = 0°$ and $\gamma = 90°$. When $\gamma = 0°$, there is a large SHF in the broadband range of band I and band II, while the numerical value and frequency range of SHF obviously decrease when $\gamma = 90°$. This causes a drastic change in the heat flux, resulting in a large MC. When $\varepsilon_s = 3$, the SHF at $\gamma = 90°$ has little change compared to that of $\varepsilon_s = 1$. But at $\gamma = 0°$, the frequency range of SHF obviously shrinks, and the value of SHF decreases compared to that of $\varepsilon_s = 1$. Therefore, the total heat flux for $\varepsilon_s = 3$ at $\gamma = 0°$ decreases, resulting in a reduction in MC. When $\varepsilon_s = 10$, the SHF in band I and band II is minimal, there is little difference between the SHFs at $\gamma = 0°$ and $\gamma = 90°$, resulting in a small MC. When $\gamma = 90°$, the SHF in band III for $\varepsilon_s = 10$ is obviously higher than that of $\varepsilon_s = 1$ and $\varepsilon_s = 3$, which results in a larger heat flux at $\gamma = 90°$ for $\varepsilon_s = 10$ in Fig. 4. It is noteworthy that in band III, the SHFs at $\gamma = 0°$ and $\gamma = 90°$ are almost identical, indicating that rotation does not affect the heat flux in band III. As ε_s increases, the heat flux in band III increases, but the contribution of it is relatively small, while the heat flux in band I and band II decreases more significantly with the increase of ε_s. Therefore, the total heat flux diminishes with the increase of ε_s, which explains the difference in the total heat flux shown in Fig. 4. Moreover, as ε_s increases, the proportion of heat flux in band III to the total heat flux becomes progressively larger, which to some extent weakens the difference of total heat flux at $\gamma = 0°$ and $\gamma = 90°$, leading to a smaller MC.

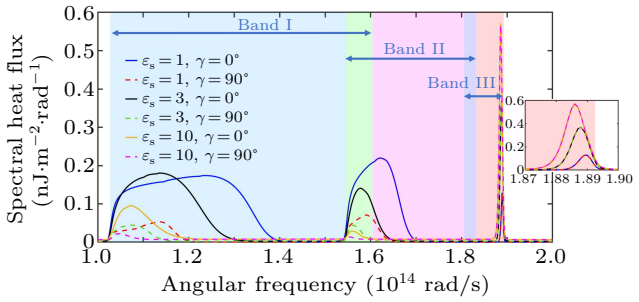


Fig. 5. Spectral heat fluxes at $\gamma = 0°$ and $\gamma = 90°$ with substrate permittivity of $\varepsilon_s = 1$, 3 and 10. $t = 10$ nm.

To further understand the mechanisms behind the changes of spectral heat flux at $\gamma = 0°$ and $\gamma = 90°$, we investigate the imaginary parts of reflection coefficient Im (r_{pp}) and the ETCs at typical angular frequencies. Firstly, we select the peak frequency of spectral heat flux in band I for analysis. Figure 6 plots the Im (r_{pp}) and ETCs of α-MoO_3 films for $\varepsilon_s = 3$ at 1.14×10^{14} rad/s. The permittivity components of α-MoO_3 at this angular frequency are $\varepsilon_x = 7.5530 + j0.028$, $\varepsilon_y = -27.0727 + j1.1357$ and $\varepsilon_z = 2.7924 + j0.0009$. Based on the permittivities ($\varepsilon_x > 0$, $\varepsilon_y < 0$, $\varepsilon_z > 0$), the hyperbolic volume phonon polaritons (HVPPs) can be excited in the wavevector space for both upper and lower regions.[64] The boundary lines define the excitation range of HPPs, they are plotted by green solid lines and can be calculated by[65]

$$k_y = \pm\sqrt{-\frac{\varepsilon_x}{\varepsilon_y}}k_x. \tag{6}$$

Furthermore, the blue dashed lines denote the dispersion curves, they can be expressed as[66]

$$\beta = \frac{\rho}{k_0 t}\left[\arctan\left(\frac{\varepsilon_1\rho}{\varepsilon_z}\right) + \arctan\left(\frac{\varepsilon_3\rho}{\varepsilon_z}\right) + \pi l\right],$$
$$l = 0, 1, 2, \ldots, \tag{7}$$

where $\rho = j\sqrt{\varepsilon_z\beta^2/\left(\varepsilon_x k_x^2 + \varepsilon_y k_y^2\right)}$, ε_1 and ε_3 represent the permittivity of vacuum and substrate, and l is the excitation order of HPPs. The boundary lines of α-MoO_3, according to Eq. (6), are $k_y = \pm 0.53 k_x$ at 1.14×10^{14} rad/s. It is known that r_{pp} is related to the state density of photons, which characterizes the magnitude of absorbed energy. In the following figures, it can be observed that the excitation region and topological shape of HPPs are consistent with that of Im (r_{pp}), and they match well with the boundary lines and dispersion curves.

We calculate the Im (r_{pp}) of the emitter in Fig. 6(a). It is evident that the state density of photons can be enhanced both above and below the origin of wavevector space. When the receiver is not rotated ($\gamma = 0°$), the Im (r_{pp}) of the receiver shown in Fig. 6(b) coincides with that of the emitter. Therefore, in Fig. 6(c), large areas of enhanced ETCs can be observed above and below the origin of wavevector space, which contributes to a large heat flux. It can be seen that the dispersion curves are distributed in the middle of the bright bands, indicating the dominant role of HVPPs in the photon tunneling. Furthermore, as shown in Fig. 6(d), when the receiver is rotated by 90° ($\gamma = 90°$), the regions of absorbed energy rotate 90° in the wavevector space. Comparing Figs. 6(a) and 6(d), there is a mismatch in the distribution area of Im (r_{pp}), the HVPPs can only be excited in small regions where Im (r_{pp}) overlap, as shown in Fig. 6(e). Although the HVPPs are excited at large wavevectors, the values of ETCs are notably small, reaching a maximum of only close to 0.2. Consequently, the heat flux for $\gamma = 90°$ is small. Therefore, rotation causes an obvious mismatch in HPPs, which explains the difference between heat fluxes for $\gamma = 0°$ and $\gamma = 90°$ at this angular frequency shown in Fig. 5(b).

Next, we plot the Im (r_{pp}) and ETCs of α-MoO_3 films for $\varepsilon_s = 10$ at 1.07×10^{14} rad/s in Fig. 7. The permittivities are $\varepsilon_x = 7.1221 + j0.0204$, $\varepsilon_y = -78.2887 + j7.1913$ and $\varepsilon_z = 2.7645 + j0.0007$. According to Ref. [64], the HVPPs can be excited both above and below the origin. The boundary lines represented by green lines are $k_y = \pm 0.30 k_x$ at this angular frequency. It can be seen in Fig. 7 that as ε_s increases

from 3 to 10, the values of Im (r_{pp}) are lower, the slope of the boundary lines and the curvature of the dispersion curves are smaller compared to that in Fig. 6. As ε_s increases, the expansion of HVPPs is inhibited and shrinks to a thin bright band, as shown in Fig. 7(c), resulting in a decrease in heat flux. In Fig. 7(e), the dispersion curves intersect at lower wavevector due to the decrease in curvature, leading to a smaller excitation wavevector for HVPPs compared to that in Fig. 6(e). However, the overlapping area of Im (r_{pp}) at $\gamma = 0°$ and $\gamma = 90°$ becomes larger, in other words, the mismatch phenomenon is weakened. Thus, in Fig. 7(e), there is a larger bright area for excited HVPPs in the wavevector space, and the values of ETCs are higher. As a result, when $\varepsilon_s = 10$, the heat flux for $\gamma = 0°$ decreases, while the heat flux for $\gamma = 90°$ increases compared to that of $\varepsilon_s = 3$, leading to a reduction in MC, which explains why MC reduces with the increase of ε_s.

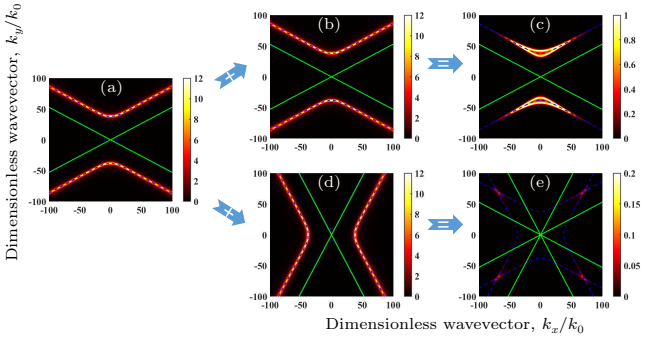


Fig. 6. Variations in the imaginary part of r_{pp} with dimensionless wavevector for the (a) emitter when $\gamma = 0°$, and receiver when (b) $\gamma = 0°$ and (d) $\gamma = 90°$. Variations in ETCs with dimensionless wavevector when (c) $\gamma = 0°$ and (e) $\gamma = 90°$. Here, $t = 10$ nm, $\varepsilon_s = 3$, $\omega = 1.14 \times 10^{14}$ rad/s.

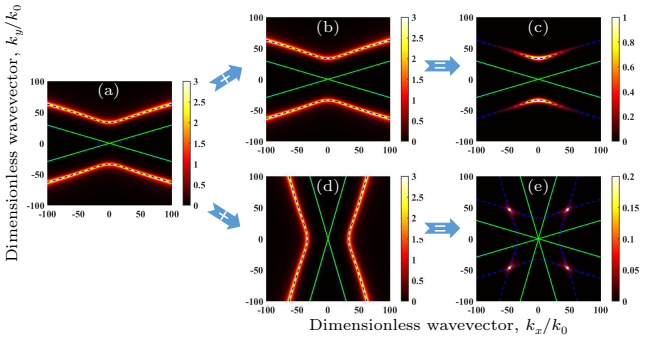


Fig. 7. Variations in imaginary part of r_{pp} with dimensionless wavevector for (a) emitter when $\gamma = 0°$, and receiver when (b) $\gamma = 0°$ and (d) $\gamma = 90°$. Variations in ETCs with dimensionless wavevector when (c) $\gamma = 0°$ and (e) $\gamma = 90°$. Here, $t = 10$ nm, $\varepsilon_s = 10$, $\omega = 1.07 \times 10^{14}$ rad/s.

Then, we select the peak frequency of spectral heat flux in band II for analysis. We plot the Im (r_{pp}) and ETCs of α-MoO_3 films for $\varepsilon_s = 3$ at 1.58×10^{14} rad/s in Fig. 8. The permittivity components of α-MoO_3 at this angular frequency are $\varepsilon_x = -31.6310 + j3.955$, $\varepsilon_y = -0.2765 + j0.0453$ and $\varepsilon_z = 3.4067 + j0.0078$. According to Ref. [64], the HVPPs can be excited at all azimuthal angles, due to the limited thickness of the film, the HVPPs are excited on the left and right sides for $\varepsilon_x \gg \varepsilon_y$. From Fig. 8(e), it can be seen that HVPPs are also heavily excited at this frequency, and ETCs exhibit a large area of bright bands in the wavevector space. Therefore, at this frequency, there is a huge heat flux close to that at 1.14×10^{14} rad/s. Although the position of HVPPs excitation is different, the mismatch phenomenon of HVPPs after rotating the receiver is also analogous to that in Fig. 6. However, the values of ETCs in Fig. 6(e) is relatively large, with a maximum energy close to 0.5, which makes the heat flux at $\gamma = 90°$ greater than that at 1.14×10^{14} rad/s. Therefore, the difference between heat fluxes at $\gamma = 0°$ and $\gamma = 90°$ is smaller than that at 1.14×10^{14} rad/s, but still, the variation of heat flux at this frequency also contributes to the large MC.

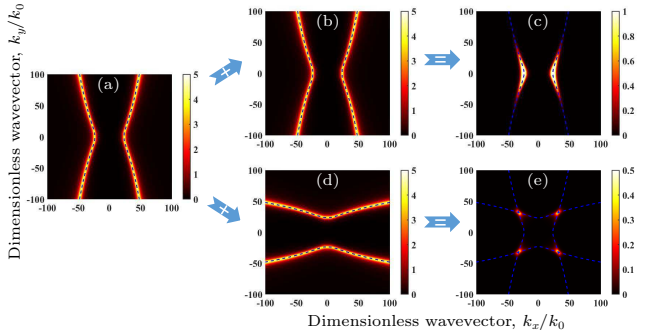


Fig. 8. Variations in imaginary part of r_{pp} with dimensionless wavevector for (a) emitter when $\gamma = 0°$, and receiver when (b) $\gamma = 0°$ and (d) $\gamma = 90°$. Variations in ETCs with dimensionless wavevector when (c) $\gamma = 0°$ and (e) $\gamma = 90°$. Here, $t = 10$ nm, $\varepsilon_s = 3$, $\omega = 1.58 \times 10^{14}$ rad/s.

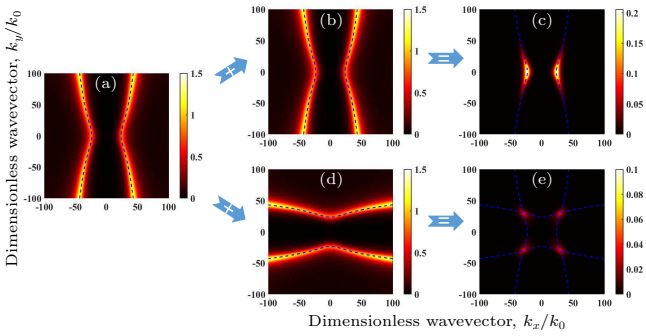


Fig. 9. Variations in imaginary part of r_{pp} with dimensionless wavevector for (a) emitter when $\gamma = 0°$, and receiver when (b) $\gamma = 0°$ and (d) $\gamma = 90°$. Variations in ETCs with dimensionless wavevector when (c) $\gamma = 0°$ and (e) $\gamma = 90°$. Here, $t = 10$ nm, $\varepsilon_s = 10$, $\omega = 1.56 \times 10^{14}$ rad/s.

Next in Fig. 9, we discuss the Im (r_{pp}) and ETCs of α-MoO_3 films for $\varepsilon_s = 10$ at 1.56×10^{14} rad/s. The permittivities at this angular frequency are $\varepsilon_x = -77.2739 + j21.4705$, $\varepsilon_y = -0.5260 + j0.0489$ and $\varepsilon_z = 3.3303 + j0.0066$. As with $\omega = 1.58 \times 10^{14}$ rad/s, the HVPPs are excited on the left and right sides. It can be seen in Fig. 9(c) that the excitation intensity of HVPPs is weak, the values of PTCs are only close to 0.2. This results in limited heat flux generation, which explains the small heat flux in band II as seen in Fig. 5. When $\gamma = 90°$, the excitation of HVPPs in Fig. 9(e) becomes weaker and can be almost ignored, resulting in a very small heat flux close to zero at this frequency. Although the variation in excitation of HVPPs is significant for $\gamma = 0°$ and $\gamma = 90°$, the

generated heat fluxes are both too small, so the difference in heat fluxes is not significant and its contribution to MC is also limited.

Moreover, the Im (r_{pp}) and ETCs of α-MoO_3 films for $\varepsilon_s = 3$ at 1.888×10^{14} rad/s (peak frequency in band III) are plotted in Fig. 10. The permittivities at this angular frequency are $\varepsilon_x = 0.7072 + j0.0399$, $\varepsilon_y = 2.0547 + j0.0178$ and $\varepsilon_z = -0.1329 + j0.0594$. According to Ref. [64], the HVPPs can be excited at all azimuth angles. In Figs. 10(a), 10(b), and 10(d), the Im (r_{pp}) exhibits a circular distribution in the wavevector space for both $\gamma = 0°$ and $\gamma = 90°$, and highly overlap. Owing to the excitation of HVPPs at all azimuth angles, the ETCs remain nearly unchanged after rotation, as seen in Figs. 10(c) and 10(e). Besides, ETCs are enhanced in a large region of wavevector space. Thus, the rotation does not affect the heat flux, there are equally large heat fluxes for $\gamma = 0°$ and $\gamma = 90°$ at this frequency, which has a reducing effect on MC. Since the Im (r_{pp}) and ETCs in band III are basically the same before and after rotation, we will not repeat the analysis of Im (r_{pp}) and ETCs in band III in the following text.

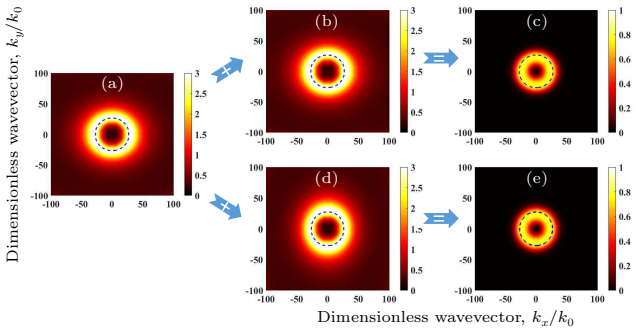


Fig. 10. Variations in imaginary part of r_{pp} with dimensionless wavevector for (a) emitter when $\gamma = 0°$, and receiver when (b) $\gamma = 0°$ and (d) $\gamma = 90°$. Variations in ETCs with dimensionless wavevector when (c) $\gamma = 0°$ and (e) $\gamma = 90°$. Here, $t = 10$ nm, $\varepsilon_s = 3$, $\omega = 1.888 \times 10^{14}$ rad/s.

3.2. Substrate effect of lossy substrate

In addition, we also consider the effect of lossy substrate and discuss the impact of variation in imaginary component of ε_s on MC. As shown in Fig. 11(a), when heat flux follows [010] crystal orientation, the MCs of $\varepsilon_s = 3 + j0.01$ and $\varepsilon_s = 3 + j0.1$ are reduced compared to that of $\varepsilon_s = 3$, and demonstrate a trend of initial increase followed by subsequent decrease with varying film thickness, similar to that of $\varepsilon_s = 3$. When the imaginary component of ε_s is small (i.e., $\varepsilon_s = 3 + j0.01$), the MC is very close to that of $\varepsilon_s = 3$, and reaches a maximum value of 4.60 at $t = 10$ nm. As the imaginary component of ε_s increases to 1, the decrease in MC becomes more pronounced, and the MC becomes monotonically increasing with film thickness. As shown in Fig. 11(b), when heat flux follows [100] crystal orientation, the variation trend of MC with the imaginary component of ε_s is similar to that of the [010] case. In Fig. 11(c), when heat flux follows [001] crystal orientation, the MC monotonically increases with film thickness for both lossless and lossy substrates, and tends to stabilize when the film thickness approaches 100 nm. The results indicate that when the real component of permittivity is equal, the reducing effect of lossy substrate on MC is stronger than that of lossless substrate. As the imaginary component of ε_s increases, the reduction of the MC becomes more significant. Similarly, we take the example of NFRHT following [010] crystal orientation of α-MoO_3 to analyze the reasons for the effect of the imaginary component of ε_s on the MC.

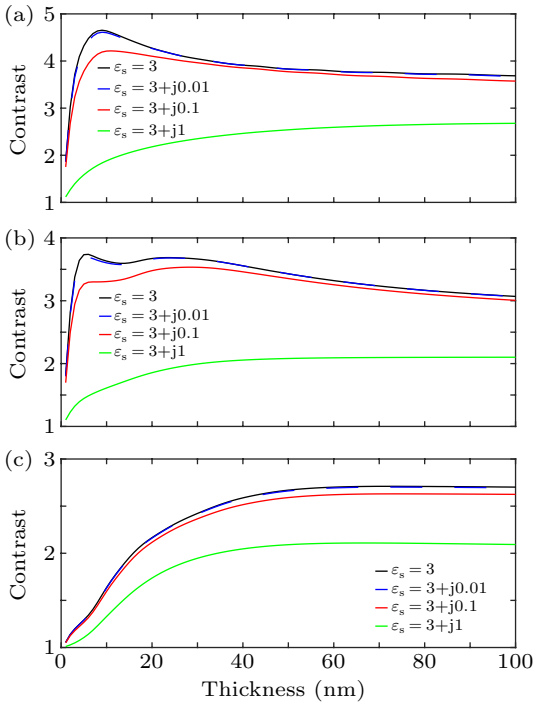


Fig. 11. Variation in modulation contrast with α-MoO_3 film thickness when NFRHT follows (a) [010], (b) [100], and (c) [001] crystal orientations. The substrate permittivities are $\varepsilon_s = 3$, $3 + j0.01$, $3 + j0.1$, and $3 + j1$.

To explain the differences in the MCs with different imaginary components of ε_s, we analyze the variation in total heat flux with rotation angle γ in Fig. 12, with the film thickness of $t = 10$ nm. When $\gamma = 0°$, the heat fluxes of $\varepsilon_s = 3$, $3 + j0.01$, and $3 + j0.1$ are very close, approximately 4.43 kW/m^2. With increasing rotation angle, the heat flux of $\varepsilon_s = 3 + j0.01$ is nearly identical to that of $\varepsilon_s = 3$, so the MCs are nearly equal. While the heat flux of $\varepsilon_s = 3 + j0.1$ increases compared to that of $\varepsilon_s = 3$ and $3 + j0.01$, resulting in a decrease in MC shown in Fig. 11(a). For $\varepsilon_s = 3 + j1$, the heat flux at $\gamma = 0°$ is smaller compared to that of other three cases, but the heat flux after rotation is obviously larger, and reaching 2 kW/m^2 at $\gamma = 90°$, which makes the difference between heat fluxes at $\gamma = 0°$ and $\gamma = 90°$ smaller, causing further decline in MC.

Moreover, we investigate the spectral heat flux at $\gamma = 0°$ and $\gamma = 90°$ with different imaginary components of ε_s, to explain the difference in total heat flux before and after rotation. As shown in Fig. 13, when $\varepsilon_s = 3 + j0.01$, the distri-

bution of SHF is nearly consistent with the situation of $\varepsilon_s = 3$ in Fig. 5(b), which explains the identical total heat flux with $\varepsilon_s = 3$ and $\varepsilon_s = 3 + \mathrm{j}0.01$ in Fig. 12. This indicates that small imaginary component of ε_s has almost no impact on the heat flux. When $\varepsilon_s = 3 + \mathrm{j}1$, the distribution area of SHF at $\gamma = 0°$ shrinks compared to that of $\varepsilon_s = 3$, leading to a smaller heat flux. However, the SHF at $\gamma = 90°$ increases obviously compared to that of $\varepsilon_s = 3$, resulting in a greater heat flux. The variation in SHF after rotation explains the comparison of heat flux in Fig. 12. As the imaginary component of ε_s increases, the difference in heat fluxes between $\gamma = 0°$ and $\gamma = 90°$ decreases, leading to a decrease in MC. It is worth noting that in band III, the SHFs at $\gamma = 0°$ and $\gamma = 90°$ are nearly identical, and hardly change with the imaginary component of ε_s, indicating that rotation and the imaginary component of ε_s do not affect the SHF in band III.

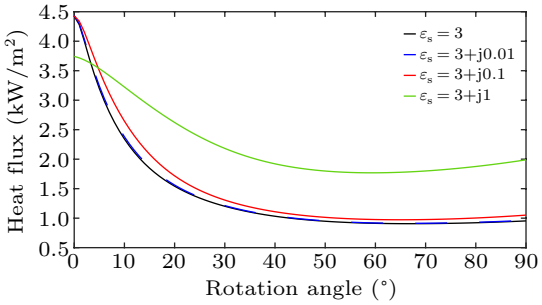


Fig. 12. Variation in heat flux with rotation angle. The substrate permittivities are $\varepsilon_s = 3$, $3 + \mathrm{j}0.01$, $3 + \mathrm{j}0.1$, and $3 + \mathrm{j}1$. $t = 10$ nm.

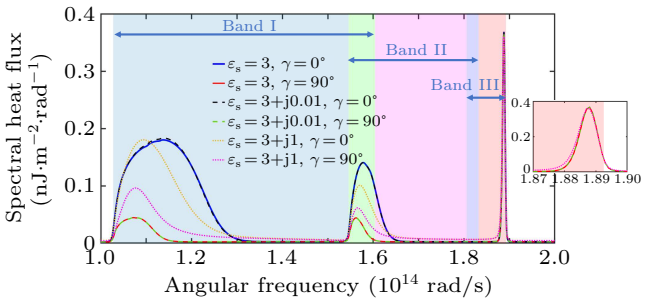


Fig. 13. Spectral heat fluxes at $\gamma = 0°$ and $\gamma = 90°$ with substrate permittivity of $\varepsilon_s = 3$, $3 + \mathrm{j}0.01$ and $3 + \mathrm{j}1$. $t = 10$ nm.

Next, we plot the Im (r_{pp}) and ETCs of α-MoO_3 films for $\varepsilon_s = 3 + \mathrm{j}1$ at 1.1×10^{14} rad/s (peak frequency in band I) in Fig. 14. The permittivities are $\varepsilon_x = 7.2831 + \mathrm{j}0.0231$, $\varepsilon_y = -45.6870 + \mathrm{j}2.7290$ and $\varepsilon_z = 2.7753 + \mathrm{j}0.0008$. According to Ref. [64], the excited HVPPs are distributed above and below the origin regions of the wavevector space. The boundary lines represented by green lines are $k_y = \pm 0.40 k_x$ at this angular frequency. In Figs. 14(a), 14(b) and 14(d), the Im (r_{pp}) is distributed at smaller wavevector, and the slope of the boundary lines and the curvature of the dispersion curves are smaller compared to that in Fig. 6. As shown in Fig. 14(c), when $\gamma = 0°$, the HVPPs can only be excited in wavevector smaller than $50k$, but the excitation area is large, which makes the amount of excited HVPPs considerable. Therefore, although the position and topological shape of excited HVPPs are different from Fig. 6(c), the heat flux contributed by HVPPs is basically the same, which leads to a nearly similar peak heat flux in band I for $\varepsilon_s = 3$ and $\varepsilon_s = 3 + \mathrm{j}1$ in Fig. 13. As shown in Fig. 14(e), when $\gamma = 90°$, due to the reduction in the slope of the dispersion curves, the HVPPs are distributed in the region of small wavevector. However, due to the loss in substrate, the excitation range of HVPPs has expanded, forming a continuous region, and the values of the ETCs are larger than that in Fig. 6(e). Therefore, when $\gamma = 90°$, the heat flux for $\varepsilon_s = 3 + \mathrm{j}1$ significantly increases compared to that for $\varepsilon_s = 3$, the presence of loss in substrate increases the heat flux when $\gamma = 90°$, narrowing the difference in heat flux compared to $\gamma = 0°$, which explains the reason for the decrease in MC.

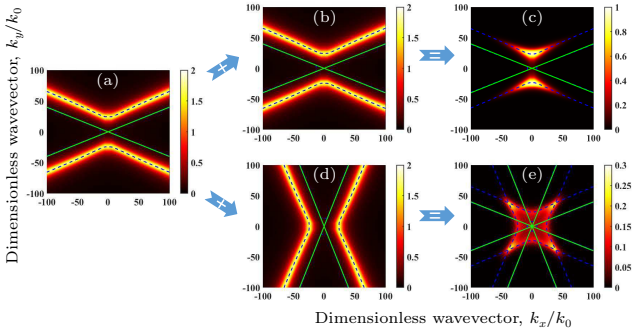


Fig. 14. Variations in imaginary part of r_{pp} with dimensionless wavevector for (a) emitter when $\gamma = 0°$, and receiver when (b) $\gamma = 0°$ and (d) $\gamma = 90°$. Variations in ETCs with dimensionless wavevector when (c) $\gamma = 0°$ and (e) $\gamma = 90°$. Here, $t = 10$ nm, $\varepsilon_s = 3 + \mathrm{j}1$, $\omega = 1.1 \times 10^{14}$ rad/s.

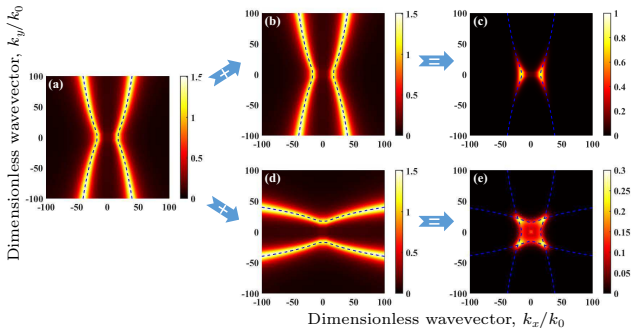


Fig. 15. Variations in imaginary part of r_{pp} with dimensionless wavevector for (a) emitter when $\gamma = 0°$, and receiver when (b) $\gamma = 0°$ and (d) $\gamma = 90°$. Variations in ETCs with dimensionless wavevector when (c) $\gamma = 0°$ and (e) $\gamma = 90°$. Here, $t = 10$ nm, $\varepsilon_s = 3 + \mathrm{j}1$, $\omega = 1.57 \times 10^{14}$ rad/s.

Finally, we plot the Im (r_{pp}) and ETCs of α-MoO_3 films for $\varepsilon_s = 3 + \mathrm{j}1$ at 1.57×10^{14} rad/s (peak frequency in band II) in Fig. 15. The permittivities are $\varepsilon_x = -45.8401 + \mathrm{j}7.7809$, $\varepsilon_y = -0.3989 + \mathrm{j}0.0470$ and $\varepsilon_z = 3.3668 + \mathrm{j}0.0072$. Similar to the previous analysis of $\omega = 1.58 \times 10^{14}$ rad/s, the HVPPs are excited on the left and right sides. As can be seen, the region of excited HVPPs in Fig. 15(c) is nearly the same as that in Fig. 8(c), different from the entire bright band in Fig. 8(c), the values of ETCs in Fig. 15(c) are obviously smaller, leading to a decrease in heat flux. When $\gamma = 90°$, the range of

excited HVPPs is continuous, filling the area enclosed by the dispersion curves. Therefore, although the values of ETCs are not as large as in Fig. 8(c), the amount of excited HVPPs is large, leading to enhanced heat flux. As a result, the heat flux with lossy substrate decreases when $\gamma = 0°$ and increases when $\gamma = 90°$, which explains why MC decreases as the imaginary part of ε_s increases.

4. Conclusion

We have studied the influence of substrate effect on near-field radiative modulators based on α-MoO_3. The results show that compared to the situation without a substrate, the presence of both lossless and lossy substrate will reduce the MC of α-MoO_3 films, regardless of the orientation of NFRHT. For lossless substrates, the decrease in MC is more significant when ε_s is larger. For lossy substrates with the same real component of ε_s, the MC decreases as the imaginary component of ε_s increases. This is because as the real or imaginary component of ε_s increases, the mismatch of HPPs weakens, resulting in a smaller difference in heat flux before and after rotation. When ε_s is large, the MC will be very small. By reducing the real and imaginary components of ε_s, the MC can significantly improve and reach 4.64 for $\varepsilon_s = 3$ at $t = 10$ nm. Choosing substrate with a smaller permittivity helps to achieve better modulation effect, which provides guideline for substrate selection in the design of near-field radiative modulators. This study offers theoretical insights guiding the application of natural hyperbolic materials in near-field thermal radiation devices.

Acknowledgments

Project supported by the National Natural Science Foundation of China (Grant No. 52106099), the Natural Science Foundation of Shandong Province of China (Grant No. ZR2022YQ57), and the Taishan Scholars Program.

References

[1] Polder D and Hove M 1971 *Phys. Rev. B* **4** 3303
[2] Basu S, Zhang Z M and Fu C J 2009 *Int. J. Energy Res.* **33** 1203
[3] Hu L, Narayanaswamy A, Chen X and Chen G 2008 *Appl. Phys. Lett.* **92** 133106
[4] St-Gelais R, Guha B, Zhu L X, Fan S H and Lipson M 2014 *Nano Lett.* **14** 6971
[5] Lim M, Song J, Lee S S and Lee B J 2018 *Nat. Commun.* **9** 4302
[6] Shi K Z, Sun Y C, Chen Z Y, He N, Bao F L, Evans J and He S L 2019 *Nano Lett.* **19** 8082
[7] Du W, Yang J, Zhang S, Iqbal N, Dang Y D, Xu J B and Ma Y G 2020 *Nano Energy* **78** 105264
[8] Lu L, Zhang B, Ou H, Li B W, Zhou K, Song J L, Luo Z X and Cheng Q 2022 *Small* **18** 2108032
[9] Sabbaghi P, Long L S, Ying X Y, Lambert L, Taylor S, Messner C and Wang L P 2020 *J. Appl. Phys.* **128** 025305
[10] Zhang W B, Wang B X and Zhao C Y 2022 *Int. J. Heat Mass Transf.* **188** 122588
[11] Song J L, Lu L, Li B W, Zhang B, Hu R, Zhou X P and Cheng Q 2020 *Int. J. Heat Mass Transf.* **150** 119346
[12] Shi K Z, Chen Z Y, Xu X N, Evans J and He S L 2021 *Adv. Mater.* **33** 2106097
[13] Liu H T, Yu K, Zhang K H, Ai Q, Xie M and Wu X H 2023 *Int. J. Heat Mass Transf.* **210** 124206
[14] Zhou C L, Wu X H, Zhang Y and Yi H L 2022 *Int. J. Heat Mass Transf.* **183** 122140
[15] Luo M G, Zhao J M, Liu L H and Antezza M 2020 *Phys. Rev. B* **102** 024203
[16] Song J L, Cheng Q, Zhang B, Lu L, Zhou X P, Luo Z X and Hu R 2021 *Rep. Prog. Phys.* **84** 036501
[17] Wu H H, Liu X C, Cai Y P, Cui L J and Huang Y 2022 *Mater. Today Phys.* **27** 100825
[18] Tang L, DeSutter J and Francoeur M 2020 *ACS Photonics* **7** 1304
[19] Zhang W B, Zhao C Y and Wang B X 2019 *Phys. Rev. B* **100** 075425
[20] Zheng Z H and Xuan Y M 2011 *Nanosc. Microsc. Therm.* **15** 237
[21] Hu Y, Sun Y S, Zheng Z H, Song J L, Shi K Z and Wu X H 2022 *Int. J. Heat Mass Transf.* **189** 122666
[22] Zhang J H, Liu H T, Yang B, Hu Y, Sun Y S and Wu X H 2023 *Phys. Chem. Chem. Phys.* **25** 1133
[23] Biehs S A, Messina R, Venkataram P S, Rodriguez A W, Cuevas J C and Ben-Abdallah P 2021 *Rev. Mod. Phys.* **93** 025009
[24] Castillo-Lopez S G, Esquivel-Sirvent R, Villarreal C and Pirruccio G 2022 *Appl. Phys. Lett.* **121** 201708
[25] Hajian H, Rukhlenko I D, Erçağlar V, Hanson G and Ozbay E 2022 *Appl. Phys. Lett.* **120** 112204
[26] Walter L P and Francoeur M 2022 *Appl. Phys. Lett.* **121** 182206
[27] Wen S Z, Dang C Z and Liu X L 2022 *Appl. Phys. Lett.* **121** 071101
[28] Fang J L, Qu L, Zhang Y and Yi H L 2023 *Int. J. Heat Mass Transf.* **200** 123515
[29] Yu Z Q, Li X P, Lee T and Iizuka H 2022 *Int. J. Heat Mass Transf.* **197** 123339
[30] Song J, Han J, Choi M and Lee B 2022 *Sol. Energy Mater. Sol. Cells* **238** 111556
[31] Yang Z M, Li H D, Wang Y, Chen X H and Chen J C 2022 *Energy Convers. Manage.* **257** 115416
[32] Zhang Y S, Li K, Yang X D, Cao S W, Pang H Q, Cai Q L, Ye Q and Wu X 2022 *Int. J. Thermophys.* **43** 1
[33] Chen F Q, Liu X J, Tian Y P, Goldsby J and Zheng Y 2022 *Energies* **15** 1830
[34] Chen K F, Santhanam P and Fan S H 2015 *Appl. Phys. Lett.* **107** 091106
[35] Fan D J, Burger T, McSherry S, Lee B, Lenert A and Forrest S R 2020 *Nature* **586** 237
[36] Li L, Yu K, Feng D D, Yang Z M, Zhang K H, Liu Y F and Wu X H 2023 *Phys. Rev. Appl.* **20** 064015
[37] Yang B and Dai Q 2022 *Nanoscale* **14** 16978
[38] Jing L, Li Z, Salihoglu H, Liu X and Shen S 2022 *Mater. Today Phys.* **29** 100921
[39] Landrieux S, Ben-Abdallah P and Messina R 2022 *Appl. Phys. Lett.* **120** 143502
[40] Guclu C, Campione S and Capolino F 2011 *Phys. Rev. B* **86** 205130
[41] Chen K F, Santhanam P and Sandhu S 2015 *Phys. Rev. B* **91** 134301
[42] Liu X L and Zhang Z M 2016 *Nano Energy* **26** 353
[43] van Zwol P J, Joulain K, Ben-Abdallah P, Greffet J J and Chevrier J 2011 *Phys. Rev. B* **83** 201404
[44] Moncada-Villa E, Fernández-Hurtado V, García-Vidal F J, García-Martín A and Cuevas J C 2015 *Phys. Rev. B* **92** 125418
[45] Shi K Z, Chen Z Y, Xing Y X, Yang J X, Xu X N, Evans J S and He S L 2022 *Nano Lett.* **22** 7753
[46] Biehs S A, Rosa F S S and Ben-Abdallah P 2011 *Appl. Phys. Lett.* **98** 243102
[47] Tang G M, Chen J and Zhang L 2021 *ACS Photonics* **8** 443
[48] Zhang Y, Yi H L and Tan H P 2018 *ACS Photonics* **5** 3739
[49] Luo M G, Zhao J M and Antezza M 2020 *Appl. Phys. Lett.* **117** 053901
[50] He M J, Qi H, Ren Y T, Zhao Y J and Antezza M 2020 *Int. J. Heat Mass Transf.* **150** 119305
[51] He M J, Qi H, Ren Y T, Zhao Y J and Antezza M 2020 *Opt. Lett.* **45** 2914
[52] Liu X L, Shen J D and Xuan Y M 2017 *J. Quant. Spectrosc. Radiat. Transf.* **200** 100
[53] Wu X H and Fu C J 2021 *Int. J. Heat Mass Transf.* **168** 120908
[54] Li L, Wu X H, Liu H T, Shi K Z, Liu Y K and Yu K 2023 *Int. J. Heat Mass Transf.* **216** 124603
[55] Wu X H, Fu C J and Zhang Z M 2018 *J. Photon. Energy* **9** 032702
[56] Wu X H, Fu C J and Zhang Z M 2020 *J. Heat Transf.* **142** 072802

[57] Ma W L, Alonso-González P, Li S J, Nikitin A Y, Yuan J, Martín-Sánchez J, Taboada-Gutiérrez J, Amenabar I, Li P N, Vélez S, Tollan C, Dai Z G, Zhang Y P, Sriram S, Kalantar-Zadeh K, Lee S T, Hillenbrand R and Bao Q L 2018 *Nature* **562** 557

[58] Ye M, Qiang B, Zhu S, Dai M J, Wang F K, Luo Y, Wang Q and Wang Q J 2022 *Adv. Opt. Mater.* **10** 2102096

[59] Huang J W, Tao L, Dong N N, Wang H Q, Zhou S, Wang J, He X Y and Wu K H 2023 *Adv. Opt. Mater.* **11** 2202048

[60] Biehs S A, Ben-Abdallah P, Rosa F S S, Joulain K and Greffet J J 2011 *Opt. Express* **19** A1088

[61] Francoeur M, Mengüç M P and Vaillon R 2010 *J. Appl. Phys.* **107** 034313

[62] Francoeur M, Mengüç M P and Vaillon R 2010 *J. Phys. D Appl. Phys.* **43** 075501

[63] Francoeur M, Mengüç M P and Vaillon R 2011 *Phys. Rev. B* **84** 075436

[64] Wu X H and Liu R Y 2020 *ES Energy Environ.* **10** 66

[65] Wu X H and Fu C J 2021 *J. Quant. Spectrosc. Radiat. Transf.* **258** 107337

[66] Álvarez-Pérez G, Voronin K V, Volkov V S, Alonso-González P and Nikitin A Y 2019 *Phys. Rev. B* **100** 235408